The Astrophysical Journal Supplement Series, 269:43 (19pp), 2023 December https://doi.org/10.3847/1538-4365/ad0298

JWST's PEARLS: Transients in the MACS J0416.1−2403 Field

Haojing Yan[1], Zhiyuan Ma[2], Bangzheng Sun[1], Lifan Wang[3], Patrick Kelly[4], José M. Diego[5], Seth H. Cohen[6], Rogier A. Windhorst[6,7], Rolf A. Jansen[6], Norman A. Grogin[8], John F. Beacom[9,10,11], Christopher J. Conselice[12], Simon P. Driver[13], Brenda Frye[14], Dan Coe[8], Madeline A. Marshall[15,16], Anton Koekemoer[8], Christopher N. A. Willmer[14], Aaron Robotham[13], Jordan C. J. D'Silva[13], Jake Summers[6], Mario Nonino[17], Nor Pirzkal[8], Russell E. Ryan, Jr.[8], Rafael Ortiz, III[6], Scott Tompkins[6], Rachana A. Bhatawdekar[18], Cheng Cheng[19], Adi Zitrin[20], and S. P. Willner[21]

[1] Department of Physics and Astronomy, University of Missouri, Columbia, MO 65211, USA
[2] Department of Astronomy, University of Massachusetts, Amherst, MA 01003, USA
[3] George P. and Cynthia Woods Mitchell Institute for Fundamental Physics & Astronomy, Texas A&M University, Department of Physics and Astronomy, 4242 TAMU, College Station, TX 77843, USA
[4] School of Physics and Astronomy, University of Minnesota, 116 Church Street SE, Minneapolis, MN 55455, USA
[5] Instituto de Física de Cantabria (CSIC-UC), Avda. Los Castros s/n, E-39005, Santander, Spain
[6] School of Earth & Space Exploration, Arizona State University, Tempe, AZ 85287-1404, USA
[7] Department of Physics, Arizona State University, Tempe, AZ 85287-1504, USA
[8] Space Telescope Science Institute, 3700 San Martin Drive, Baltimore, MD 21218, USA
[9] Center for Cosmology and AstroParticle Physics (CCAPP), The Ohio State University, Columbus, OH 43210, USA
[10] Department of Physics, The Ohio State University, Columbus, OH 43210, USA
[11] Department of Astronomy, The Ohio State University, Columbus, OH 43210, USA
[12] Jodrell Bank Centre for Astrophysics, Alan Turing Building, University of Manchester, Oxford Road, Manchester M13 9PL, UK
[13] International Centre for Radio Astronomy Research (ICRAR) and the International Space Centre (ISC), The University of Western Australia, M468, 35 Stirling Highway, Crawley, WA 6009, Australia
[14] Steward Observatory, University of Arizona, 933 N Cherry Avenue, Tucson, AZ, 85721-0009, USA
[15] National Research Council of Canada, Herzberg Astronomy & Astrophysics Research Centre, 5071 West Saanich Road, Victoria, BC V9E 2E7, Canada
[16] ARC Centre of Excellence for All Sky Astrophysics in 3 Dimensions (ASTRO 3D), Australia
[17] INAF-Osservatorio Astronomico di Trieste, Via Bazzoni 2, I-34124 Trieste, Italy
[18] European Space Agency, ESA/ESTEC, Keplerlaan 1, 2201 AZ Noordwijk, The Netherlands
[19] Chinese Academy of Sciences South America Center for Astronomy, National Astronomical Observatories, CAS, Beijing 100101, People's Republic of China
[20] Physics Department, Ben-Gurion University of the Negev, P.O. Box 653, Beer-Sheva 8410501, Israel
[21] Center for Astrophysics | Harvard & Smithsonian, 60 Garden Street, Cambridge, MA 02138, USA
Received 2023 July 14; revised 2023 October 9; accepted 2023 October 10; published 2023 November 22

Abstract

With its unprecedented sensitivity and spatial resolution, the James Webb Space Telescope (JWST) has opened a new window for time-domain discoveries in the infrared. Here we report observations in the only field that has received four epochs (spanning 126 days) of JWST NIRCam observations in Cycle 1. This field is toward MACS J0416.1−2403, which is a rich galaxy cluster at redshift $z = 0.4$ and is one of the Hubble Frontier Fields. We have discovered 14 transients from these data. Twelve of these transients happened in three galaxies (with $z = 0.94$, 1.01, and 2.091) crossing a lensing caustic of the cluster, and these transients are highly magnified by gravitational lensing. These 12 transients are likely of a similar nature to those previously reported based on the Hubble Space Telescope (HST) data in this field, i.e., individual stars in the highly magnified arcs. However, these 12 could not have been found by HST because they were too red and too faint. The other two transients are associated with background galaxies ($z = 2.205$ and 0.7093) that are only moderately magnified, and they are likely supernovae. They indicate a demagnified supernova surface density, when monitored at a time cadence of a few months to a ∼3–4 μm survey limit of AB ∼28.5 mag, of ∼0.5 arcmin^{-2} integrated to $z \approx 2$. This survey depth is beyond the capability of HST but can be easily reached by JWST.

Unified Astronomy Thesaurus concepts: Transient sources (1851); Infrared sources (793); Gravitational lensing (670); Supernovae (1668); Surveys (1671)

1. Introduction

New capabilities in multimessenger and time-domain astronomy will open outstanding vistas for discovery, as highlighted, for example, in the Decadal Survey on Astronomy and Astrophysics 2020 (Astro2020).[22] A core challenge is in localizing sources on the sky and in redshift, with the primary technique being searches for electromagnetic counterparts, which calls for observatories with the best flux sensitivity and angular resolution possible.

Until recently, one of the leading observatories for this purpose was the Hubble Space Telescope (HST), which has had many successes. For example, it has found high-redshift supernovae (SNe), especially those of type Ia, which constrain cosmological models. In many cases, these observations were integrated with large, general-purpose extragalactic surveys (e.g., Riess et al. 2004; Amanullah et al. 2010; Suzuki et al. 2012; Riess et al. 2018). Observations of high-redshift clusters

[22] https://nap.nationalacademies.org/resource/26141/interactive/

have been important for increasing yields (e.g., Dawson et al. 2009; Hayden et al. 2021), while observations of low-redshift clusters have led to the first discovery of a supernova (SN) that is gravitationally lensed into multiple images (Kelly et al. 2015, 2016). The light curves of such SNe, and in particular, the time delay between images, provide a new route to measure the Hubble–Lemaître constant H_0 (Grillo et al. 2018, 2020; Vega-Ferrero et al. 2018; Kelly et al. 2023a, 2023b). Another example is a novel type of transient phenomenon—caustic-crossing transients—has been identified through HST observations (Kelly et al. 2018; Rodney et al. 2018; Chen et al. 2019; Kaurov et al. 2019). These are individual stars in highly magnified background galaxies lying very close to the critical curve of the lensing cluster, which are further magnified—temporarily—by intracluster stars that act as microlenses. These transients have provided a completely unexpected method to study individual stars at cosmological distances.

The advent of the James Webb Space Telescope (JWST) has brought dramatically better opportunities because of its more than an order of magnitude sensitivity increase relative to HST. The Prime Extragalactic Areas for Reionization and Lensing Science program (PEARLS; Windhorst et al. 2023), one of the programs under the JWST Interdisciplinary Scientists' Guaranteed Time Observations (GTO), has a major time-domain science component. One of its fields is MACS J0416.1−2403 (hereafter M0416), which is a lensing cluster at $z \sim 0.4$ and one of the Hubble Frontier Fields (HFF; Lotz et al. 2017). The redshift of M0416 as a whole is still uncertain at the level of ± 0.003, mainly because this is a merging cluster whose subcomponents might have large peculiar motions. Spectroscopic campaigns on this cluster are described by Balestra et al. (2016), Bergamini et al. (2021), Caminha et al. (2017), and Vanzella et al. (2021). We adopt $z = 0.397$ as the fiducial redshift of this cluster. HST has previously revealed several caustic-crossing transients near two caustic-straddling arcs in M0416. Rodney et al. (2018) discovered two fast transients in an arc identified at $z = 1.0054$ (Caminha et al. 2017; Rodney et al. 2018), which was nicknamed "Spock" by the authors. The transient sources themselves are consistent with being supergiant stars with temperatures between 3500 and 18,000 K residing in the strongly lensed galaxy that constitutes the Spock arc (Diego et al. 2023a). Chen et al. (2019) and Kaurov et al. (2019) found a transient of a similar nature in another arc identified at $z = 0.94$ (Hoag et al. 2016; Caminha et al. 2017), which is named "Warhol." In addition, the ultradeep, UV-to-visible HST program "Flashlights" detected two high-significance caustic transients in the Spock arc and four in the Warhol arc (Kelly et al. 2022). Highly lensed regions such as these are expected to produce caustic transients continually.

To take advantage of opportunities enabled by JWST, PEARLS incorporated three epochs of NIRCam observations of M0416. We expected these data to be particularly powerful for detecting red supergiant stars at $z \gtrsim 1$ because red supergiants are bright at $\lambda \gtrsim 2$ μm. The design was also motivated by the possibility of detecting individual Population III stars through caustic transits at $z > 7$ (Windhorst et al. 2018). Another JWST GTO program, the CAnadian NIRISS Unbiased Cluster Survey (CANUCS; Willott et al. 2022), also observed M0416 with NIRCam in a separate epoch. All these data have been taken, making M0416 the only field in JWST Cycle 1 that has four epochs of NIRCam observations. This makes M0416 the best region in the sky to date for studying infrared transients.

This paper reports a transient search using the unique four epoch data. The search has gone beyond the aforementioned two arcs, as we also intend to assess the general infrared transient rate in less magnified regions at depths that have never been probed before. This paper is the first in a series on this subject and presents an overview of the transients found in this field. The paper is organized as follows. The NIRCam observations and data are described in Section 2. The transient search is detailed in Section 3. Section 4 discusses the transient, and Section 5 summarizes the results. All magnitudes are in the AB system, and all coordinates are in the ICRS frame (equinox 2000).

2. Observations and Data

The four epochs of NIRCam observations all used the same eight bands, namely, F090W, F115W, F150W, and F200W in the *short wavelength* (SW) channel and F277W, F356W, F410M, and F444W in the *long wavelength* (LW) channel. The native NIRCam pixel scales are $0\farcs031\ \mathrm{pix}^{-1}$ in the SW channel and $0\farcs063\ \mathrm{pix}^{-1}$ in the LW channel. As the SW channel is made up of four detectors, the observations used the `INTRAMODULEBOX` dithers to cover the gaps. The PEARLS observations adopted the `MEDIUM8` readout pattern with *up-the-ramp* fitting to determine the count rate, while those of CANUCS used a combination of the `SHALLOW4` and `DEEP8` patterns. The total exposure times, dates of observation, and 5σ depths of these observations are summarized in Table 1.

NIRCam has two nearly identical modules ("A" and "B") that subtend two adjacent, square fields. As the spatial orientations of the JWST instruments vary in time on an annual basis, these two fields cannot both be in the same region in the sky within a year. For this reason, all four epochs of NIRCam observations were designed to center the B module on the cluster, leaving the A module mapping different regions in the flanking area. This transient study uses only the module B data because only these are spatially overlapped.

The data were retrieved from the Mikulski Archive for Space Telescopes. Reduction started from the so-called Stage 1 *uncal* products, which are the single exposures from the standard JWST data reduction pipeline (Bushouse et al. 2023) after Level 1b processing. We further processed these products using the version 1.9.4 pipeline in the context of `jwst_1063.pmap`. A few changes and augmentations were made to the pipeline to improve the reduction quality; most importantly, these included enabling the use of an external reference catalog for image alignment and implementing a better background estimate for the final stacking. The astrometry of each single exposure was calibrated using the public HFF products.[23] These single images were projected onto the same grid and were stacked in each band and in each epoch. We produced two versions of stacks, one at the pixel scale of $0\farcs06$ (hereafter the "60 mas" version) and the other at the scale of $0\farcs03$ (the "30 mas" version), to best match the native pixel scales in the LW and the SW channels, respectively. The mosaics are in surface brightness units of MJy sr^{-1}. The AB magnitude zero-points are 26.581 and 28.087 for the 60 and 30 mas stacks, respectively. Figure 1 shows a composite color image using the data from all four epochs. For convenience, we refer to the

[23] https://archive.stsci.edu/prepds/frontier/macs0416.html

Table 1
M0416 NIRCam Observation Summary

Epoch Start (UT)	Filter	Exp Time (s)	Depth 5σ
Ep1	F090W	3779.343	28.45
2022 Oct 7 08:06:05	F115W	3779.343	28.48
(0.0 days)	F150W	2920.401	28.48
(PA = 293°)	F200W	2920.401	28.69
	F277W	2920.401	29.83
	F356W	2920.401	29.91
	F410M	3779.343	29.38
	F444W	3779.343	29.58
Ep2	F090W	3779.343	28.49
2022 Dec 29 16:00:36	F115W	3779.343	28.51
(83.4 days)	F150W	2920.401	28.51
(PA = 33°)	F200W	2920.401	28.72
	F277W	2920.401	29.88
	F356W	2920.401	29.93
	F410M	3779.343	29.39
	F444W	3779.343	29.59
Ec	F090W	6399.115	28.63
2023 Jan 11 20:24:42	F115W	6399.115	28.64
(96.7 days)	F150W	6399.115	28.82
(PA = 49°)	F200W	6399.115	29.02
	F277W	6399.115	30.14
	F356W	6399.115	30.19
	F410M	6399.115	29.50
	F444W	6399.115	29.70
Ep3	F090W	3779.343	28.48
2023 Feb 10 09:12:32	F115W	3349.872	28.41
(126.1 days)	F150W	2920.401	28.49
(PA = 71°)	F200W	2920.401	28.69
	F277W	2920.401	29.84
	F356W	2920.401	29.86
	F410M	3349.872	29.21
	F444W	3779.343	29.47

Note. The 5σ depths (in AB magnitudes) are measured from the rms map within circular apertures of $0\farcs2$ radius. PA is the angle of the detector y-axis projected on the sky in degrees east from north.

three epochs from the PEARLS program as Ep1, Ep2, and Ep3, respectively, where "p" stands for "PEARLS." The epoch from the CANUCS program, which was between Ep2 and Ep3, is referred to as Ec ("c" for "CANUCS").

3. Transient Discoveries

3.1. Search Method

The search for transients was done in the usual way by detecting positive peaks on difference images between epochs. Thanks to the excellent image alignment and stable image quality, we were able to form the difference images by direct subtraction, for which we used the 60 mas images. Due to the intense human labor in the visual inspection step (see below), this work is limited to these pairs of difference images: Ep1−Ep2 for the search of decaying sources in Ep1, Ep2−Ep1 for new sources appearing in Ep2, and Ep3–Ep1 for new sources appearing in Ep3. Ec was not used to initiate transient searches, as it was only 13.3 days after Ep2; however, it was used when studying the light curves of the identified transients. When building a difference image, its rms map was also constructed by adding the rms maps of the parent images in quadrature. As compared to the SW images, the LW images are less affected by defects and therefore their difference images are cosmetically cleaner. We used the F356W band as the basis of our search because its data are the deepest.

The initial transient search was to run SExtractor (Bertin & Arnouts 1996) on the 60 mas F356W difference images. The rms maps were used in the process to estimate the signal-to-noise ratios (S/N) of the peaks in the difference images. Only the peaks that have $S/N \geqslant 5$ were further considered. This left thousands of peaks in each difference image, which were then visually inspected. Not surprisingly, the vast majority of these peaks are not transient objects but are residuals caused by imperfect subtraction of bright stars and galaxies for two reasons: (1) the values of the pixels occupied by bright objects fluctuate over different epochs because of Poisson noise, which often results in positive peaks accompanied by negative peaks in a difference image; (2) the position angle of the point-spread function (PSF) is different in different epochs owing to the different field orientations. This leads to spurious sources around bright objects that appear in different positions in different epochs.

After the initial visual inspection, only a few tens of transient candidates survived. To ensure their reliability, we further required that the selected transients should be detected at $S/N \geqslant 5$ in the difference image of at least one more band in addition to F356W. Applying this requirement gave a total of 14 robust transients.

3.2. Descriptions of the Transients and Their Photometry

Our sample includes seven transients in the Warhol region, four in the Spock region, one in yet another arc, and two in other regions. Their locations are indicated in Figure 1. These objects and their photometry are described below. Their magnification factors based on the lens model of Bergamini et al. (2023, adopting their 68% confidence level intervals) are also quoted along with the photometry.

In most cases, these sources are embedded in a highly nonuniform background and/or are affected by contamination from nearby objects, and PSF fitting had to be used to obtain reliable photometry. For this purpose, the 30 mas images are more appropriate. To be consistent, we used PSF fitting for all objects on the 30 mas images, and the detailed process is explained in the Appendix.

3.2.1. Transients in the Warhol Region

Figure 2 shows the positions of the seven transients discovered in this region. The first three letters in their IDs indicate the difference images on which they were first detected in our process; for example, "Dc2" stands for the difference image constructed by subtracting the Ep2 image from the Ec image, and so on. The letter "W" indicates that these are in the Warhol region. The photometric results are listed in Table 2. Figure 3 shows three of them (`D21-W1`, `D21-W2`, and `D21-W3`) that were seen in multiple epochs, while Figure 4 shows the other four (`Dc2-W4`, `D31-W5`, `D31-W6`, `and D31-W7`) that were visible in only a single epoch.

1. `D21-W1`: This transient was visible in Ep1, reached its maximum brightness in Ep2, became fainter in Ec, and further declined in brightness in Ep3 but remained visible. It faded more rapidly in the red bands than in the blue ones. At its peak ($m_{277} = 27.10$ mag), it was the

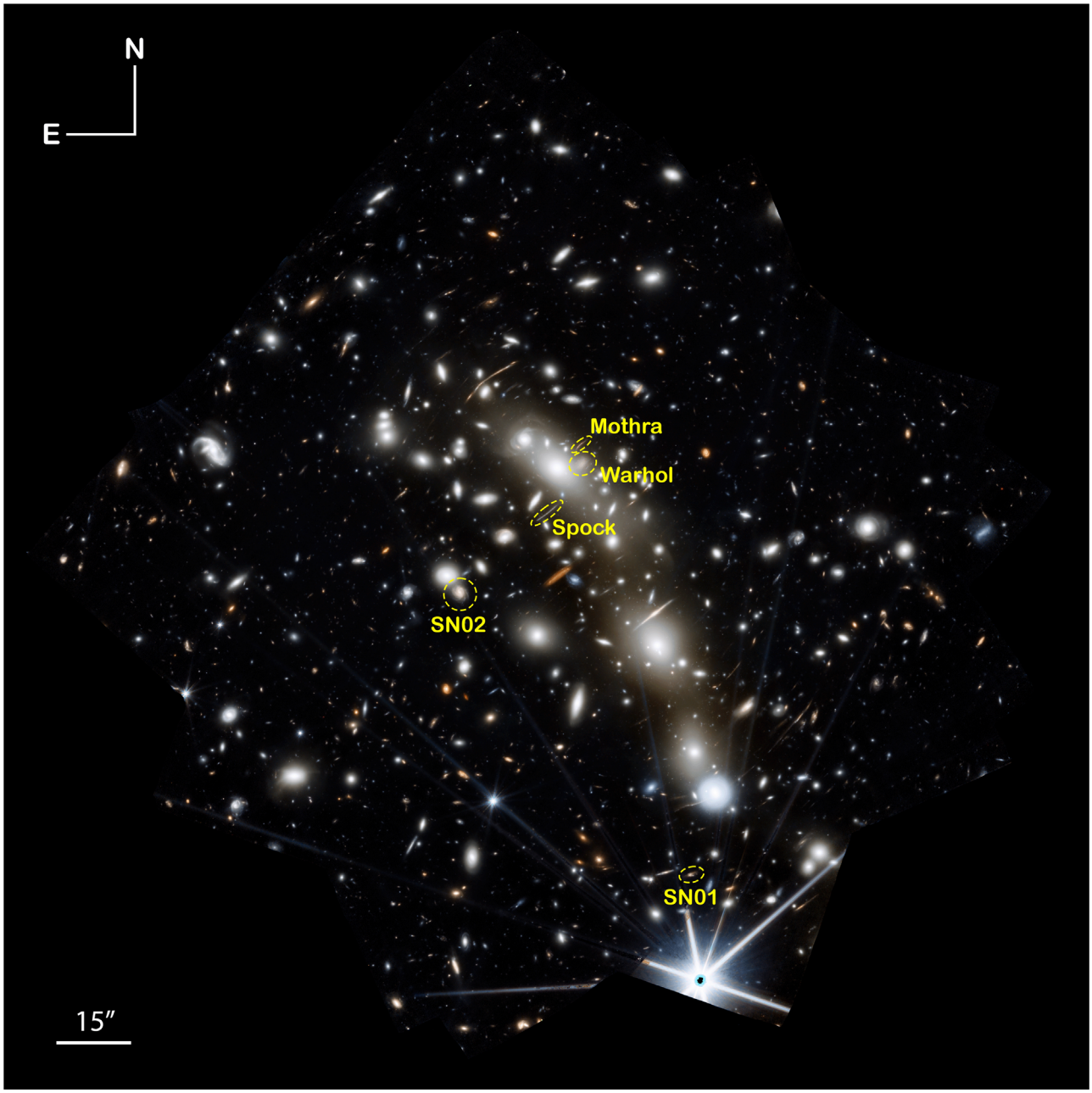

Figure 1. Color composite image of M0416 using the data from four epochs of NIRCam observations as described in the text. The color scheme is F090W+F115W +F150W as blue, F200+F277W as green, and F356W+F410M+F444W as red. The regions where the transients are found are also marked.

brightest among all transients in this region. As it was visible in all epochs, its photometry was done in each epoch individually.

2. `D21-W2`: This transient was invisible in Ep1, appeared in Ep2, and slowly varied in the following two epochs. Interestingly, its behaviors in the SW and the LW bands differed: while it decayed with time in the LW bands, it became much brighter in the SW bands in Ep3, especially in the two bluest bands. The photometry was done on the difference images between these epochs and Ep1 (i.e., the D21, Dc1, and D31 images), as this offers a more reliable determination of the background.
3. `D21-W3`: This transient was only 0.″28 away from `D21-W2` and was also invisible in Ep1. It appeared in Ep2 in F150W and redder bands. It was much weaker in Ec and barely (if at all) visible in Ep3. The photometry was done on the difference images between all other epochs and Ep1. The decline in brightness from Ep2 to Ec is very obvious in the blue bands. The F444W photometry weakly suggests that it might have slightly brightened from Ep2 to Ec, but this is inconclusive because of the large uncertainties. The extracted signals in Ep3 all have an $S/N < 2$, which we consider as non-detections.
4. `Dc2-W4`: This event appeared as a sudden brightening in Ec, particularly in the LW bands. As mentioned earlier, Ec was not used to initiate the transient search; this event was found on the difference images involving Ec when

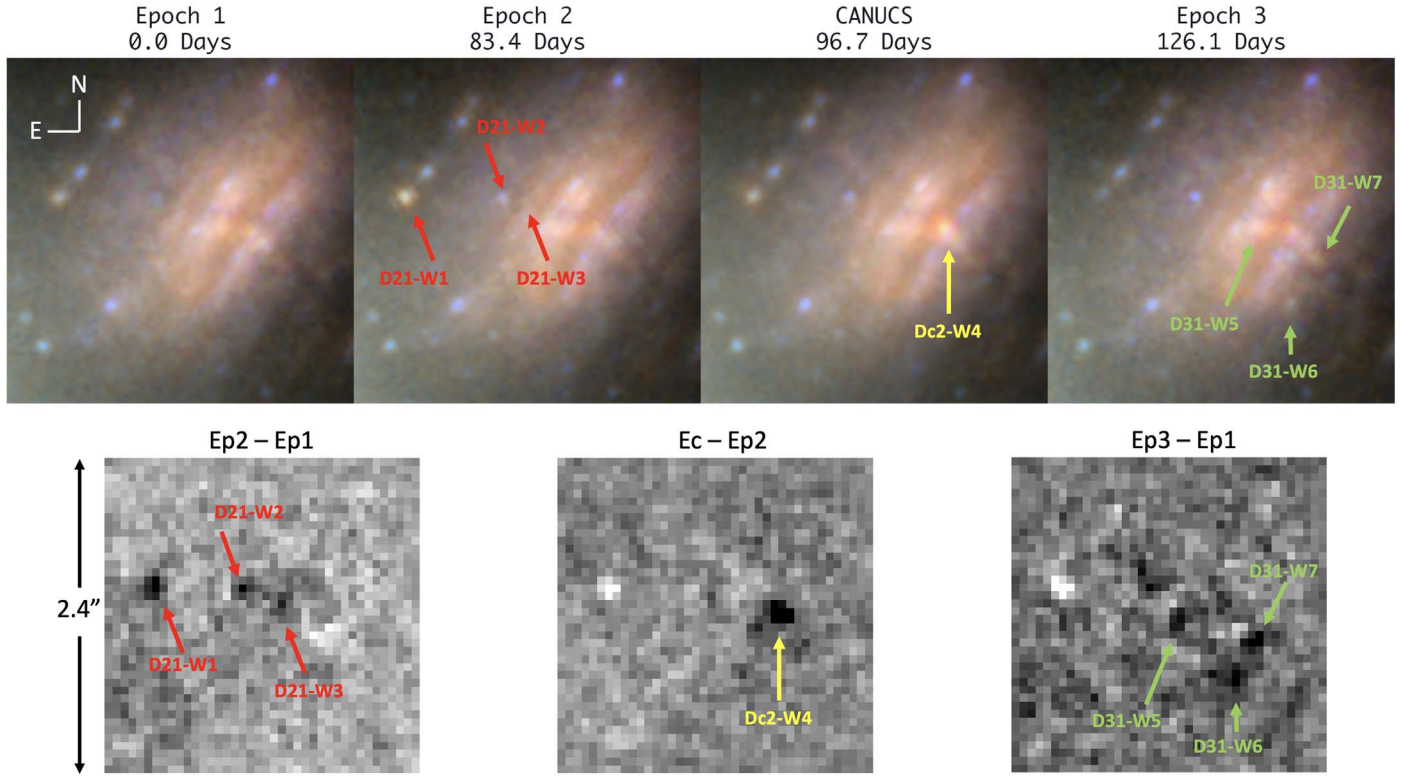

Figure 2. Locations of the transients found in the Warhol region. The upper panel shows the color images of this region in the four epochs, while the lower panels show the inverted F356W difference images of the same region between relevant epochs that led to the discovery of these transients as labeled. All these images are 2.″4 on a side and are oriented north-up and east-left.

inspecting other transients in the Warhol region. While there seems to be a *source* in other epochs at this location, there is no detectable signal in the difference images between Ep1, Ep2, and Ep3. This means that the event happened only in Ec, and it left no trace in any other epochs, including Ep2, which was only 13.3 days prior. The photometry was done on the difference images between Ec and Ep1 (i.e., the Dc1 images).

5. D31-W5: This transient was seen only in Ep3, as it was only visible in the difference images involving Ep3. It was very close to D21-W3 but was a different transient. It was invisible in the three bluest bands. The photometry was done on the difference images between Ep3 and Ep1 (the D31 images).
6. D31-W6 and D31-W7: These two transients were also seen only in Ep3. Like D31-W5, the photometry was done on the difference images between Ep3 and Ep1 (the D31 images).

3.2.2. Transients in the Spock Region

Figure 5 shows the positions of the four transients in this region. Due to the high brightness of this arc, these transients can only be revealed in the difference images, and none of them is clearly seen in the original images. Their IDs follow the convention of Section 3.2.1 with "S" to indicate that these transients are in the Spock region. Figures 6–9 show the details of these transients. Their photometry (except for D23-S3, see below) is presented in Table 3.

1. D21-S1: This transient is best detected in the difference images between Ep2 and Ep1 (the D21 images) but is seen only in the LW bands. It became significantly weaker in the difference images between Ec and Ep1 (the Dc1 images) and almost completely disappeared from those between Ep3 and Ep1 (the D31 images). All this indicates that it reached the maximum in Ep2 and then faded. Assuming that it was invisible in Ep1, we obtained its magnitudes in Ep2 and Ec by photometry on the difference images between Ep2 and Ep1 (D21) and those between Ec and Ep1 (Dc1).
2. D21-S2: This transient was detected in the difference images involving Ep2 but not otherwise. Therefore, it is reasonable to assume that this event was caught in Ep2 only. The photometry was done on the difference images between Ep2 and Ep3 (i.e., the D23 images) because this combination offers a cleaner background than others (e.g., the D21 images).
3. D23-S3: This transient was best detected in the difference images between Ep2 and Ep3 (D23). It appears in the D23 images in F150W through F410M, is barely visible in F444W, and is invisible in F115W and F090W. This transient presents a complicated case that is difficult to understand. First of all, it seems to be an elongated system in the D23 F356W image. In the D23 F200W and F150W images, which have better resolution, this elongated structure is resolved into two components. However, it does not maintain such a two-component structure (or the elongated morphology) consistently in all bands: one of the components (the southern one) is missing from the D23 F277W and F410M images. Second, in the difference images between Ep2 and Ep1 (D21), only the southern component appears, and it appears only in F200W and F150W. Taking the above at

Table 2
Catalog of Transients in the Warhol Region

	R.A.	Decl.	Epoch	F090W	F115W	F150W	F200W	F277W	F356W	F410M	F444W	μ
D21-W1	64.03695	−24.06725	Ep1	29.74 ± 0.44	28.89 ± 0.13	28.15 ± 0.06	27.90 ± 0.05	27.65 ± 0.07	27.97 ± 0.11	28.05 ± 0.12	28.46 ± 0.13	26.6
			Ep2	29.41 ± 0.19	28.68 ± 0.10	27.92 ± 0.05	27.34 ± 0.04	27.10 ± 0.05	27.19 ± 0.05	27.42 ± 0.06	27.56 ± 0.06	
			Ec	29.09 ± 0.22	28.96 ± 0.12	28.28 ± 0.06	27.78 ± 0.04	27.61 ± 0.06	27.65 ± 0.06	27.79 ± 0.07	28.08 ± 0.08	
			Ep3	29.53 ± 0.34	29.36 ± 0.35	29.03 ± 0.14	29.00 ± 0.16	29.10 ± 0.30	$>29.93^{*}$	$>29.51^{*}$	$>29.73^{*}$	
D21-W2	64.03674	−24.06725	Ep2	29.43 ± 0.21	>29.28	28.88 ± 0.16	28.99 ± 0.17	28.37 ± 0.10	28.11 ± 0.09	28.08 ± 0.11	28.83 ± 0.15	904.2
			Ec	29.26 ± 0.17	29.07 ± 0.15	29.21 ± 0.20	29.49 ± 0.25	28.53 ± 0.11	28.40 ± 0.12	28.25 ± 0.15	28.78 ± 0.18	
			Ep3	28.33 ± 0.08	28.31 ± 0.08	28.55 ± 0.11	28.89 ± 0.16	29.19 ± 0.23	28.67 ± 0.16	28.72 ± 0.20	29.09 ± 0.21	
D21-W3	64.03665	−24.06728	Ep2	>29.31	>29.28	29.72 ± 0.32	28.88 ± 0.14	28.67 ± 0.16	28.42 ± 0.12	28.69 ± 0.26	29.10 ± 0.23	331.3
			Ec	>29.40	>29.38	30.13 ± 0.46	29.78 ± 0.33	29.09 ± 0.23	28.66 ± 0.14	28.59 ± 0.21	28.77 ± 0.17	
Dc2-W4	64.03655	−24.06731	Ec	$>28.89^{*}$	$>28.87^{*}$	29.00 ± 0.19	28.18 ± 0.11	27.38 ± 0.07	27.04 ± 0.06	27.28 ± 0.06	27.36 ± 0.07	1188.6
D31-W5	64.03668	−24.06732	Ep3	>29.32	>29.29	>29.24	29.28 ± 0.22	28.75 ± 0.18	28.62 ± 0.16	28.99 ± 0.31	29.62 ± 0.39	83.0
D31-W6	64.03654	−24.06744	Ep3	>29.32	>29.29	29.13 ± 0.17	28.56 ± 0.09	28.32 ± 0.13	28.16 ± 0.10	28.17 ± 0.16	28.07 ± 0.11	62.8
D31-W7	64.03650	−24.06736	Ep3	>29.32	29.86 ± 0.34	29.71 ± 0.30	28.78 ± 0.16	28.50 ± 0.15	28.31 ± 0.12	28.64 ± 0.20	28.77 ± 0.18	365.9

Note. The R.A. and decl. coordinates are in decimal degrees for the J2000.0 equinox. The magnitudes are based on the PSF-fitting results. The upper limits are measured within 11×11 pixels (to match the size of the PSF-fitting area) centered at the source location on the rms maps. The limits labeled with $*$ are 5σ upper limits (appropriate for the measurements in the original image where the background is high and nonuniform), otherwise 2σ (more appropriate for the measurements in the difference images where the background is largely subtracted). The quoted magnification factors μ are the 68% confidence level intervals from Bergamini et al. (2023).

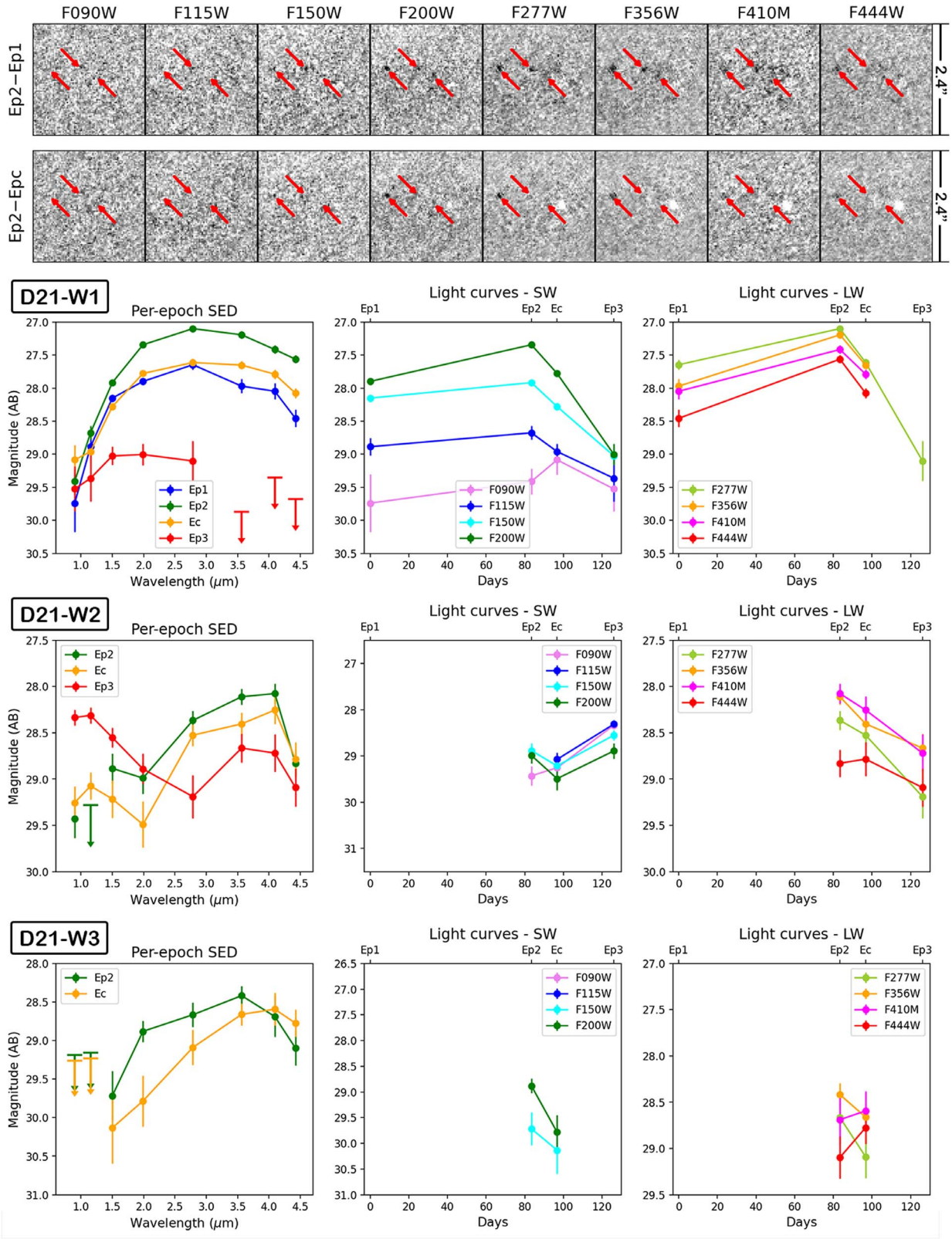

Figure 3. (Top two rows) Transients D21-W1, D21-W2, and D21-W3 in the D21 (first row) and the D2c (second row) difference images in the eight NIRCam bands as labeled. The images are 2.″4 on a side and oriented north-up and east-left. The red arrows mark the locations of transients D21-W1, D21-W2, and D21-W3 from left to right in each image. D21-W1 (visible in all epochs) is fainter in D2c (13.3 days apart) than in D21 (83.4 days apart), suggesting that it faded rapidly after reaching its maximum in Ep2. D21-W2 (not visible in Ep1) is almost invisible in Dc2, suggesting that it decayed more slowly. D21-W3 (not visible in Ep1) was similar to D21-W2 (and is only 0.″28 away) but fainter. (bottom three rows, left to right) spectral energy distributions (SEDs) in each observable epoch, light curves in the SW bands, and light curves in the LW bands. D21-W1 was visible in all epochs, and the photometry was done on the original images. The other two transients were not seen in Ep1, and their photometry was done on the difference images with respect to Ep1, i.e., the D21, Dc1, and D31 images.

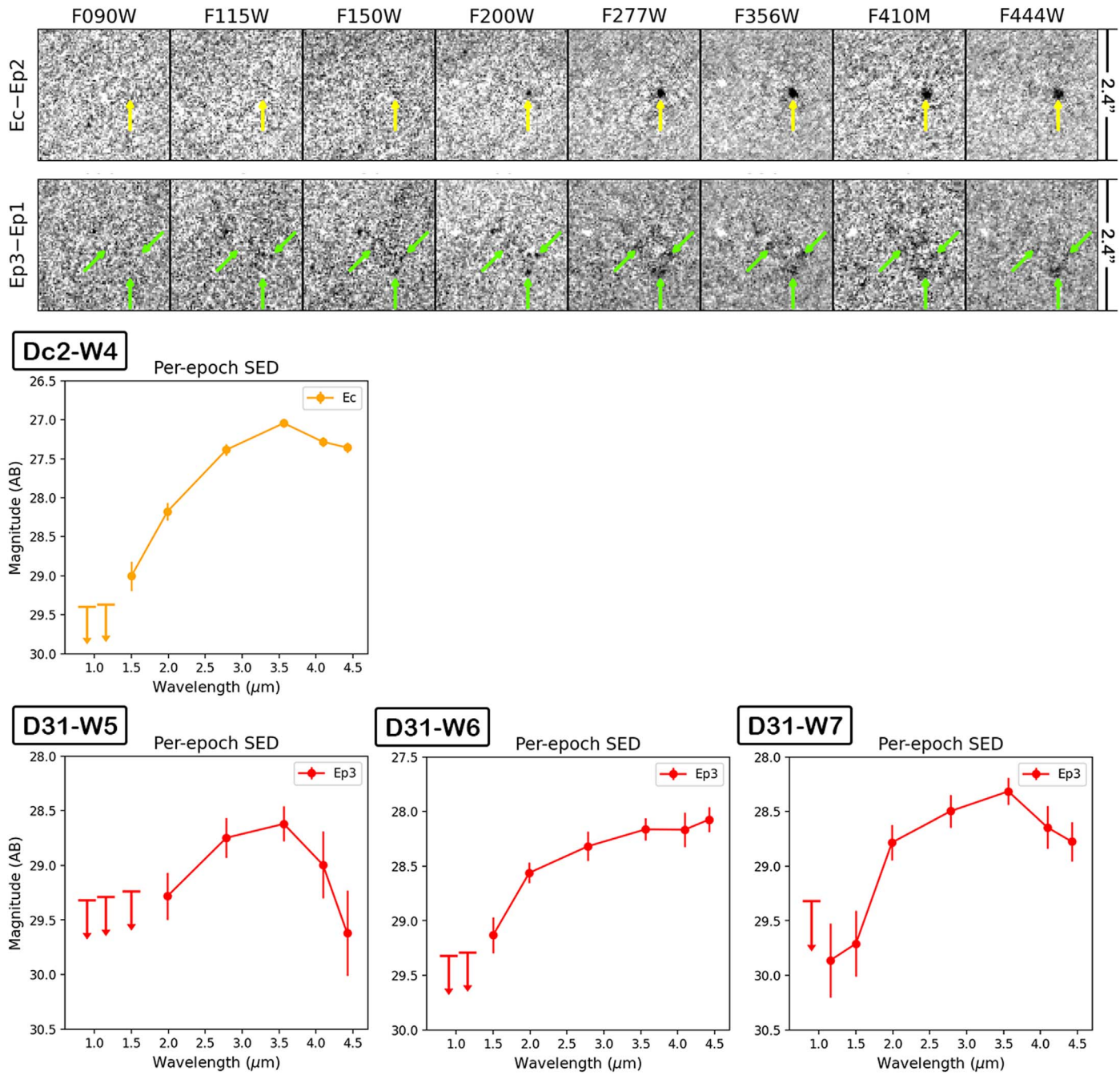

Figure 4. (Top two rows) Transients Dc2-W4 in the Dc2 difference images (first row) and D31-W5, D31-W6, and D31-W7 in the D31 difference images (second row) in eight NIRCam bands. The images are 2.″4 on a side and oriented north-up and east-left. Dc2-W4 (position marked by the yellow arrow in each image) only appeared in Ec and was not visible in any other epoch, including Ep2 only 13.3 days prior. D31-W5, D31-W6, and D31-W7 (positions marked by the green arrows from left to right in each image) were visible only in Ep3, and their detections were significant only in the LW bands. (bottom two rows) SEDs of transients Dc2-W4 and D31-W5, D31-W6, and D31-W7.

face value, one would infer the following picture: (1) D21-S3 was made of two components; (2) the northern one maintained its brightness from Ep1 to Ep2 and then decayed (not visible in the D21 images but showing up in the D23 images); (3) the southern component brightened in Ep2 but only in F150W and F200W (in the D21 images visible only in F150W and F200W) and then decayed; (4) however, this southern component maintained its brightness from Ep1 through Ep3 in F277W, F356W, and F410M. The last point is inconsistent with the observation that the southern component seems to be present in the D23 F356W image. It is possible to attribute this inconsistency to the weakness of the signals. We attempted PSF fitting on the two components in the D23 images, but the fitting failed in all bands. We had to give up photometry on this transient.

4. `D31-S4`: This transient was only detected in the difference images involving Ep3, implying that it appeared in Ep3. It is only 0.″39 away from `D21-S1`, which already decayed and was invisible in Ep3. The photometry was done on the difference images between Ep3 and Ep1 (D31).

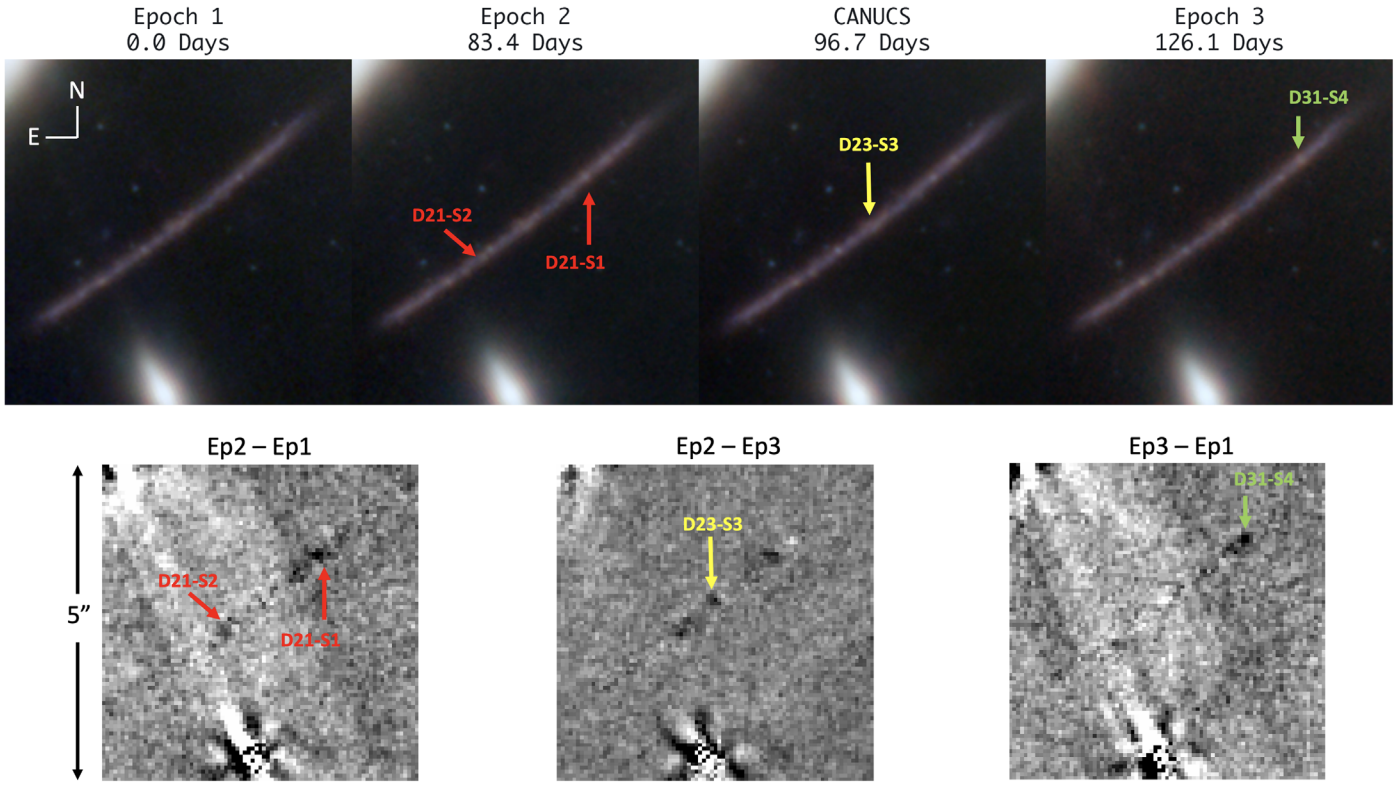

Figure 5. Locations of the transients found in the Spock region. The upper panel shows the color images of this region in the four epochs, while the lower panels show the inverted F356W difference images of the same region. All images are 5″ on a side and are oriented north-up and east-left.

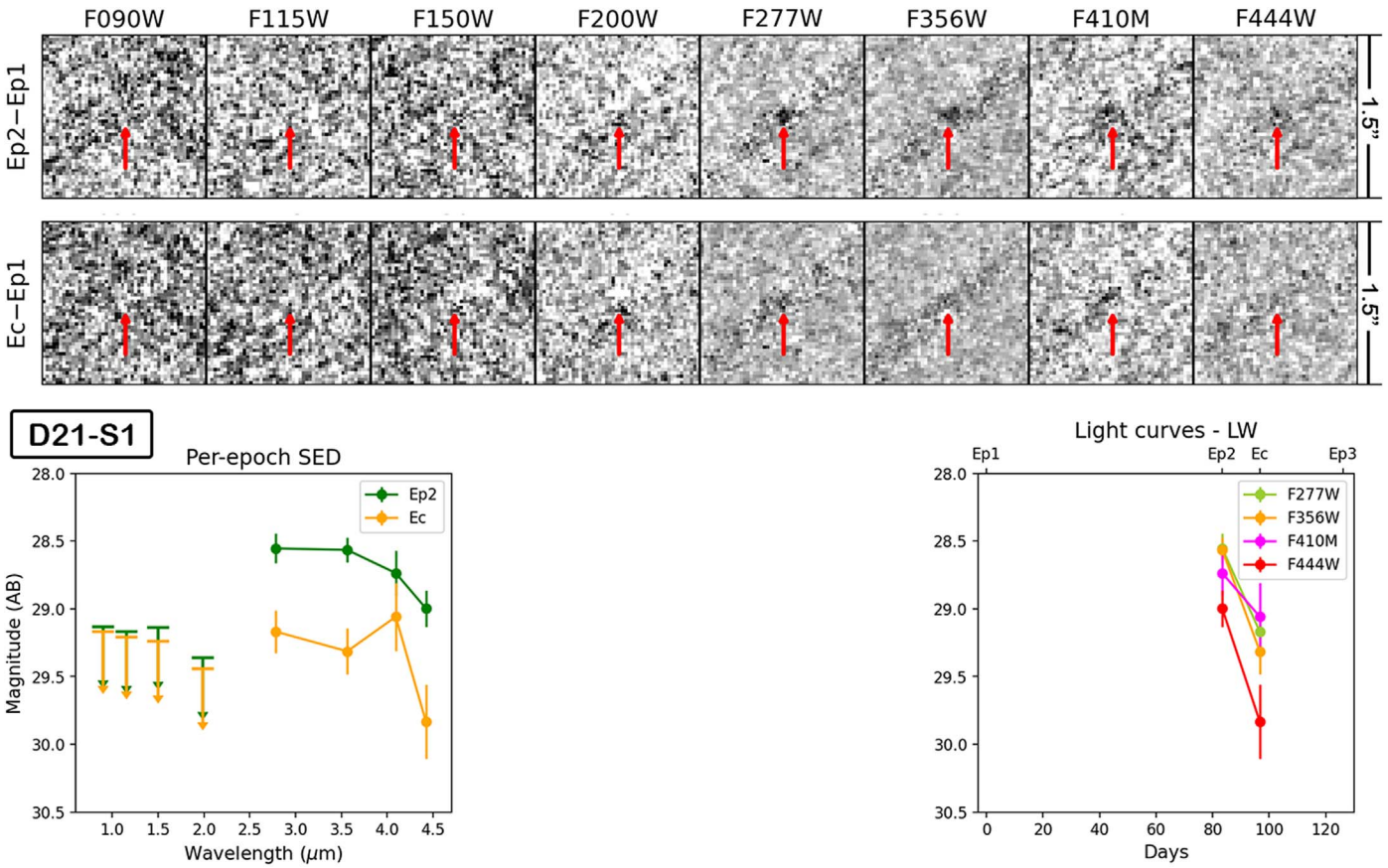

Figure 6. (Top two rows) Transient D21-S1 in the D21 (first row) and Dc1 (second row) difference images. The size of the images is labeled. The transient location is marked by the red arrow in each image. It is most prominent in the D21 images and becomes weaker in Dc1 images (but still visible), indicating that it reached maximum in Ep2 and then rapidly declined (disappearing from Ep3 entirely). It is almost invisible in the difference images in the SW bands. (Bottom row) Photometric information of this transient, similar to those presented in Figure 3 but without the light curves in SW as it was not seen in these blue bands. The photometry in Ep2 and Ec is based on the D21 and Dc1 difference images, i.e., it assumes the object was invisible in Ep1.

Table 3
Catalog of Transients in the Spock Arc Region

	R.A.	Decl.	Epoch	F090W	F115W	F150W	F200W	F277W	F356W	F410M	F444W	μ
D21-S1	64.03847	−24.06984	Ep2	>29.13	>29.17	>29.14	>29.36	28.55 ± 0.11	28.56 ± 0.09	28.74 ± 0.17	29.00 ± 0.14	612.6
			Ec	>29.17	>29.21	>29.24	>29.44	29.17 ± 0.16	29.31 ± 0.17	29.06 ± 0.25	29.83 ± 0.27	
D21-S2	64.03889	−24.07017	Ep2	>29.13	>29.17	29.65 ± 0.27	29.13 ± 0.17	28.33 ± 0.10	28.61 ± 0.12	29.12 ± 0.34	29.33 ± 0.27	87.7
D23-S3	64.03874	−24.07004										327.6
D31-S4	64.03836	−24.06978	Ep3	>29.11	29.95 ± 0.29	29.86 ± 0.33	29.06 ± 0.17	28.55 ± 0.13	28.44 ± 0.09	28.68 ± 0.20	28.49 ± 0.11	139.0

Note. As for Table 2 but for the transients in the Spock arc region. The lensing magnification factors μ are from Bergamini et al. (2023).

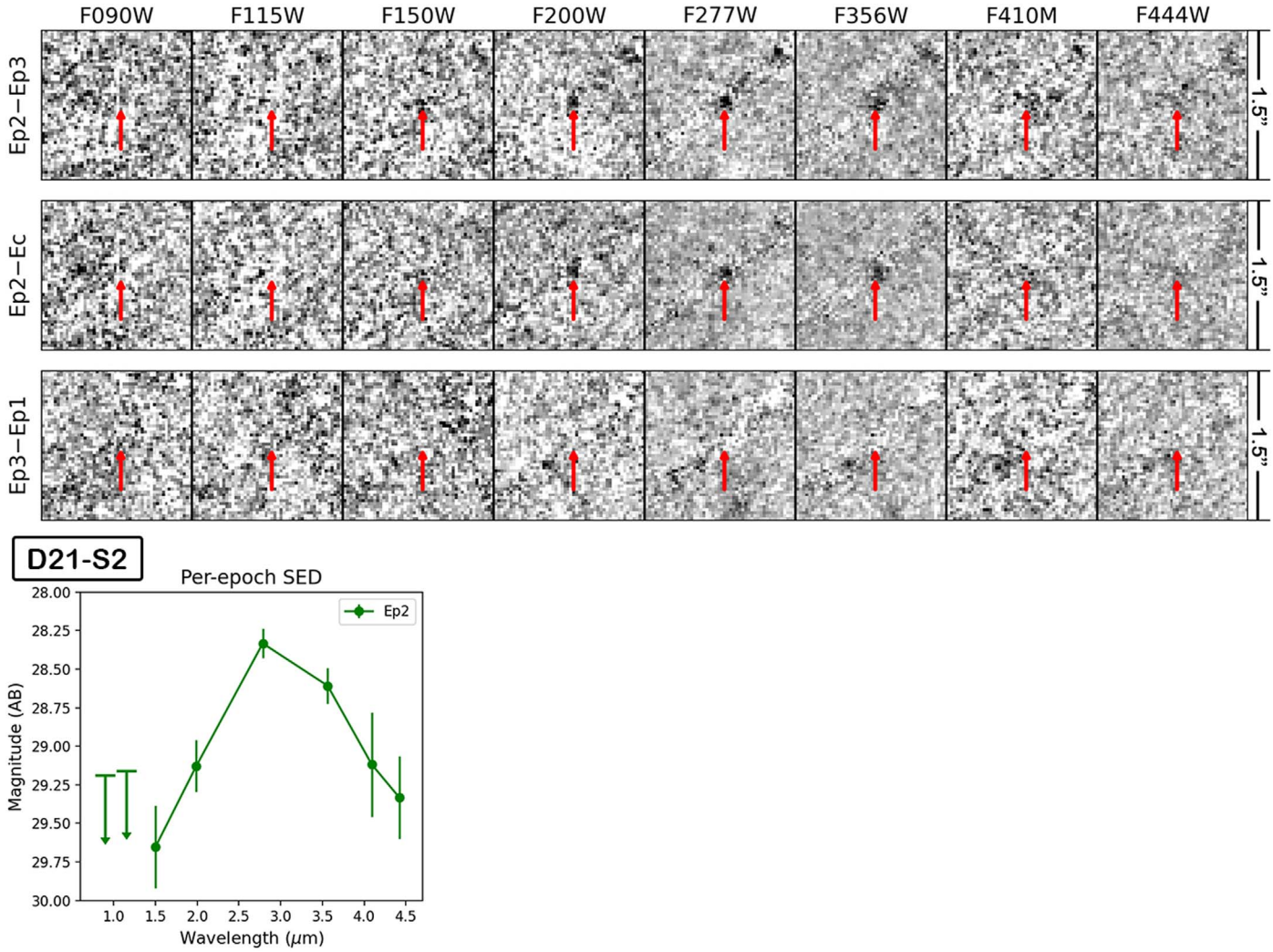

Figure 7. (Top three rows) Transient D21-S2 in the D23 (first row), D2c (second row), and D31 (third row) difference images (negative). The size of the images is labeled. The location of the transient is marked by the red arrow in each image. It is visible in the difference images involving Ep2 but not otherwise, indicating that the event was caught only in Ep2. (Bottom row) SED of the transient in Ep2 as measured from the D23 images.

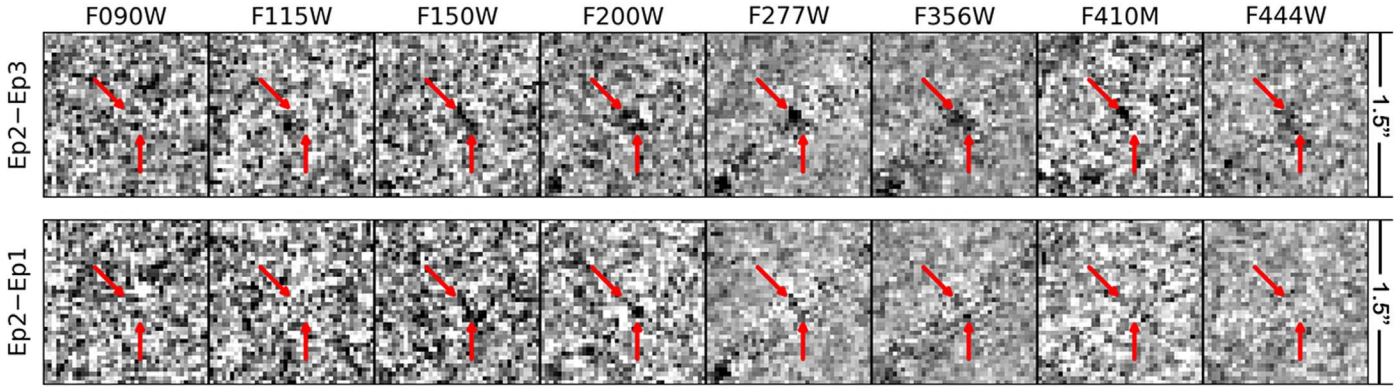

Figure 8. Transient D23-S3 in the D23 (first row) and D21 difference images. The images have the same size as labeled. The transient location is marked by the red arrow in each image. This transient, however, is the most complicated of all, and the difference images of different epoch pairs reveal some inconsistencies. See text for details.

Detecting four transients in this arc in the four epochs is consistent with expectations for this particular arc. Diego et al. (2023a) found that microlensing should produce between one and five transients per pointing in the Spock arc when reaching ∼29 mag.

3.2.3. A Transient in Yet Another Arc

There is one transient identified on an arc at $z = 2.091$ (Bergamini et al. 2021) where no previous transient has been reported. Dubbed *Mothra*, this transient is discussed in detail by Diego et al. (2023b). Figure 10 shows the details of this transient.

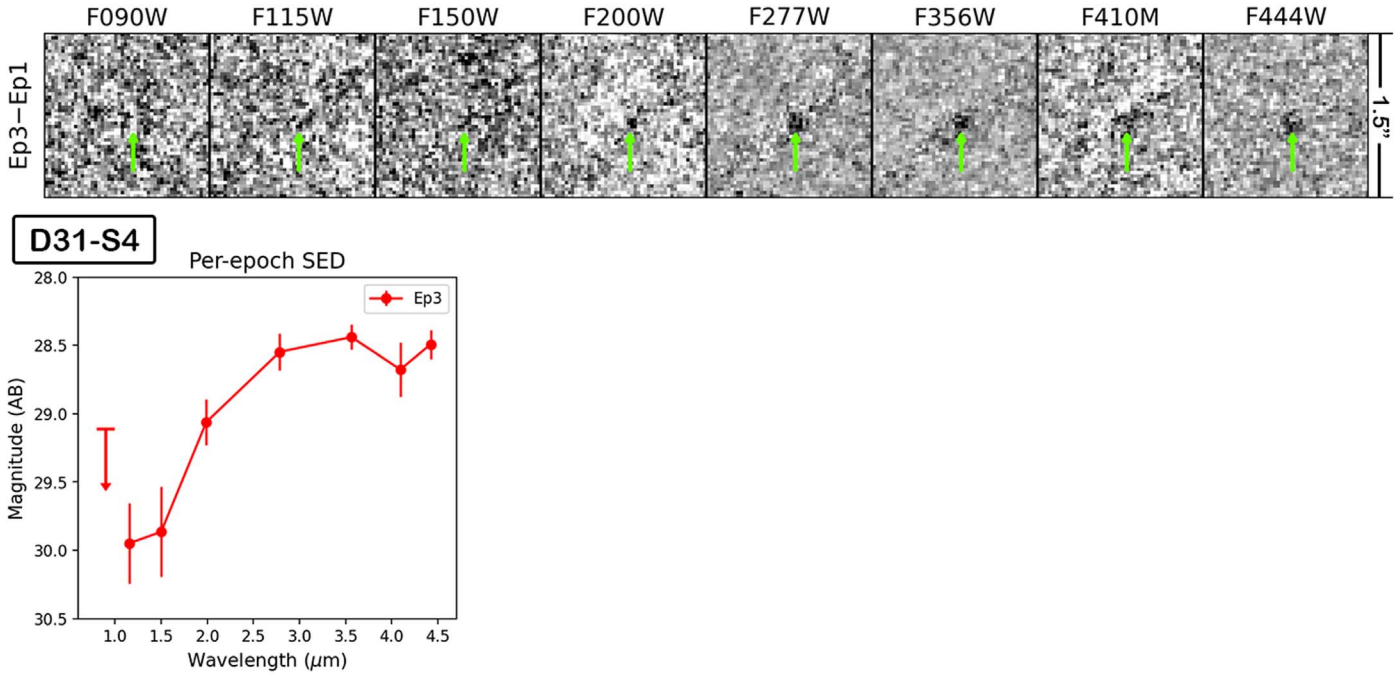

Figure 9. (Top) Transient D31-S4 in the D31 (negative) difference images. The size of the images is labeled. The transient location is marked by the green arrow in each image. It was only seen in the difference images involving Ep3, indicating that it appeared only in that epoch. (Bottom) SED of this transient in Ep3 as measured on the D31 difference images.

The knot in which it is located is the faintest among five knots on the arc, but the knot was visible in all four epochs. This transient is best explained by the intrinsic variability of a red supergiant star (in a binary system with a blue supergiant) that is being magnified by a dark millilens (Diego et al. 2023b).

The transient behavior is best seen in the difference images between Ep3 and Ep1 (D31) and as well as in those between Ec and Ep1 (Dc1), where it shows up as a strong, red source with decreasing amplitude toward the blue end. It is even visible in the difference images between Ec and Ep2 (Dc2; 13.3 days apart), albeit being much weaker. It is almost invisible in the difference images between Ep3 and Ec (D3c; 29.4 days apart). In other words, this knot was slowly increasing in brightness and reached maximum at around Ec (96.7 days between Ep1 and Ec), and it stayed more or less at its maximum through Ep3 (29.4 days between Ec and Ep3).

Because this transient was caused by the variability of a source that was visible in all epochs, ideally its photometry should be done on the images taken in each epoch. As it is almost blended with a brighter knot $0\farcs12$ to the southeast, one should do PSF fitting on both simultaneously. However, we were only able to obtain reasonable PSF-fitting results in Ep1. (The Appendix provides the details.) The procedure failed in other epochs, mostly because the light of the brightened transient blended with the nearby knot more severely. Therefore, we performed PSF fitting on the difference images between Ep1 and other epochs (Figure 10) and then added the excess fluxes extracted in this way to the Ep1 SED to obtain the SEDs in other epochs. The results are presented in Table 4 and are also shown in the bottom row of Figure 10.

3.2.4. Two Likely SNe

There were two transients associated with galaxies that are only moderately magnified. Both transients were detected in multiple epochs, and neither was seen in the HFF data. Based on their light curves, we believe that they are SNe. Their physical interpretations will be detailed in a forthcoming paper (L. Wang et al. 2023, in preparation). Their photometry is presented in Table 5.

1. SN01: We initially reported this event (Yan et al. 2023) based on the data from Ep1 and Ep2. Figure 11 shows the color images of the transient and its vicinity in the four epochs. The transient appeared as a blue source in Ep1 and then became very red in the subsequent epochs. The difference images show that its F200W and redder light reached maximum in Ep2. The source is very close to an irregular galaxy, which presumably is the host. The CANUCS NIRISS slitless spectroscopy shows that this galaxy is at $z = 2.205$ (C. Willot 2023, private communication). Because the transient was visible in all epochs, its photometry should be done on the images in individual epochs. To minimize the impact of the contamination from the host galaxy, the photometry was done by PSF fitting. The results are shown in Figure 11.
2. SN02: This transient was found within a spiral galaxy identified at $z = 0.7093$ (redshift based on Caminha et al. 2017). Figure 12 shows its color images and the difference images. The transient was invisible in Ep1 and appeared in Ep2. From the difference images, this transient was brightest in most bands in Ep2 and then slightly decayed in Ec and Ep3. The photometry in Ep2, Ec, and Ep3 was done on the difference images between Ep2 and Ep1 (D21), Ec and Ep1 (Dc1), and Ep3 and Ep1 (D31). In these difference images, the transient's neighborhood is affected by the strong residuals from imperfect subtraction of the host galaxy bulge. PSF-fitting photometry reduced but did not eliminate the contamination.

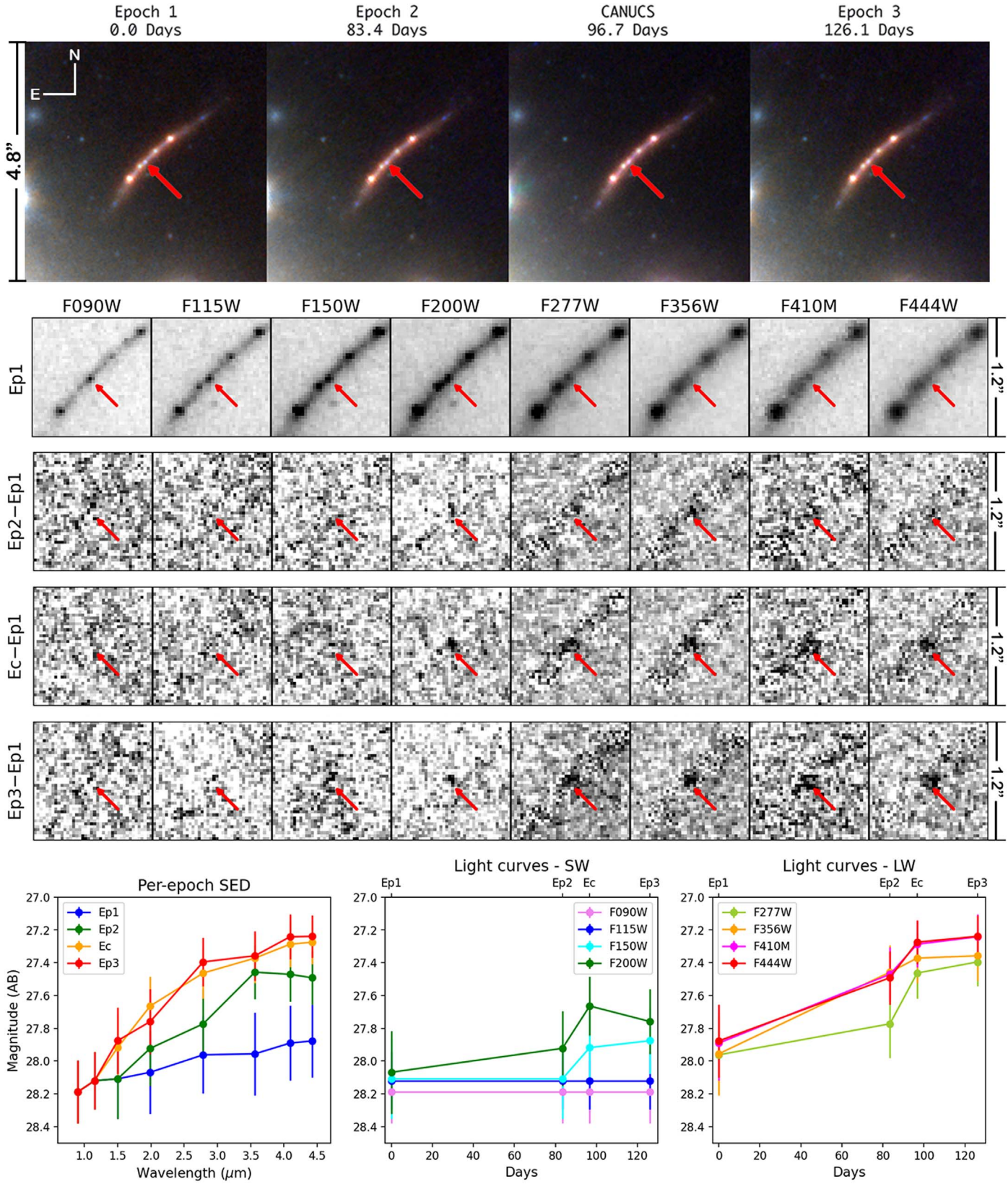

Figure 10. Mothra transient identified in an unnamed arc. The top row shows the color images (4.″8 on a side) of this region in four epochs. The red arrow in each image points to the knot that gave rise to the event. The second row zooms into the arc and shows the Ep1 images (1.″2 on a side) in the eight bands. The next three rows show the difference images between other epochs and Ep1, all displayed in negative. The last row shows the photometric information. See Section 3.2.3 and the Appendix for details of the photometry.

Table 4
Photometry for the Transient Mothra in an Arc at $z = 2.091$

R.A.	Decl.	Epoch	F090W	F115W	F150W	F200W	F277W	F356W	F410M	F444W	μ
64.03676	−24.06625	Ep1	28.19 ± 0.19	28.12 ± 0.17	28.11 ± 0.24	28.07 ± 0.25	27.96 ± 0.24	27.96 ± 0.25	27.89 ± 0.23	27.88 ± 0.22	32.5
		Ep2	28.19 ± 0.19	28.12 ± 0.17	28.11 ± 0.24	27.92 ± 0.23	27.77 ± 0.21	27.46 ± 0.16	27.47 ± 0.17	27.49 ± 0.16	
		Ec	28.19 ± 0.19	28.12 ± 0.17	27.92 ± 0.21	27.66 ± 0.18	27.46 ± 0.16	27.37 ± 0.15	27.29 ± 0.14	27.27 ± 0.13	
		Ep3	28.19 ± 0.19	28.12 ± 0.17	27.88 ± 0.20	27.76 ± 0.20	27.40 ± 0.15	27.36 ± 0.15	27.24 ± 0.14	27.24 ± 0.13	

Note. As for Table 2 but for the transient in the Mothra arc region. The lensing magnification factor μ is from Bergamini et al. (2023).

Table 5
Photometry for the Two SNe

	R.A.	Decl.	Epoch	F090W	F115W	F150W	F200W	F277W	F356W	F410M	F444W	z	μ
SN01	64.02954	−24.09022	Ep1	26.84 ± 0.05	26.85 ± 0.04	27.25 ± 0.03	27.73 ± 0.04	28.29 ± 0.07	$>29.82^{*}$	$>29.24^{*}$	$>29.49^{*}$	2.205	2.9
			Ep2	30.70 ± 0.41	29.14 ± 0.10	27.68 ± 0.04	27.16 ± 0.02	27.36 ± 0.04	27.47 ± 0.04	27.55 ± 0.05	27.64 ± 0.06		
			Ec	$>28.73^{*}$	29.76 ± 0.23	27.98 ± 0.04	27.30 ± 0.03	27.56 ± 0.04	27.55 ± 0.04	27.55 ± 0.06	27.72 ± 0.07		
			Ep3	$>28.87^{*}$	29.80 ± 0.24	28.17 ± 0.05	27.42 ± 0.03	27.63 ± 0.04	27.74 ± 0.05	27.78 ± 0.07	27.96 ± 0.08		
SN02	64.04421	−24.07449	Ep2	28.77 ± 0.11	27.85 ± 0.06	27.44 ± 0.05	27.31 ± 0.04	27.35 ± 0.06	27.60 ± 0.08	27.52 ± 0.09	27.68 ± 0.08	0.793	1.9
			Ec	29.20 ± 0.16	28.09 ± 0.06	27.62 ± 0.04	27.39 ± 0.04	27.50 ± 0.07	27.71 ± 0.07	27.85 ± 0.11	28.07 ± 0.11		
			Ep3	29.71 ± 0.31	28.04 ± 0.09	27.76 ± 0.06	27.51 ± 0.06	27.51 ± 0.08	27.54 ± 0.08	27.52 ± 0.08	27.88 ± 0.10		

Note. As for Table 2 but for the two SNe in less magnified regions. The lensing magnification factors μ are from Bergamini et al. (2023).

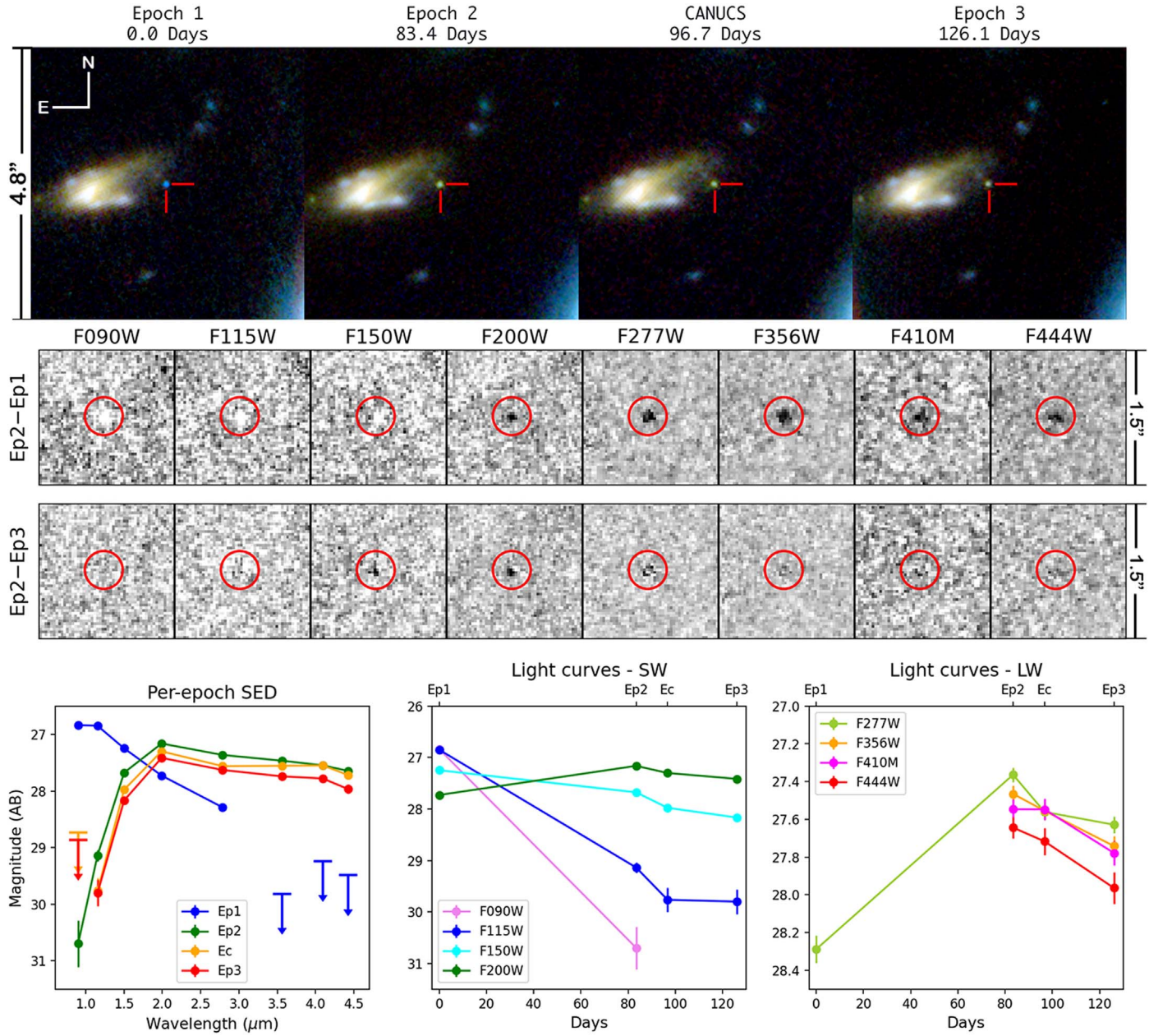

Figure 11. (Top row) Color images of SN01 in four epochs. Scale and orientation are labeled. The position of the SN is indicated by the red arrow in each image. The nearby irregular galaxy, which is at $z = 2.205$, is presumably the host. (middle two rows) D21 and D23 (negative) difference images. The location of the source is indicated by the red circle ($0\farcs5$ radius) in each image. The change in color from blue to green/yellow is obvious in the D21 images, where its location shows negative signals in the three bluest bands and positive signals in the rest. It largely maintained the same color from Ep2 through Ep3 (although becoming dimmer) as seen in the D23 images. (Bottom row) SED evolution over four epochs (left panel) and the light curves in the SW bands (middle) and the LW bands (right). In Ep1, this transient was invisible in the three reddest bands, and the downward arrows in its Ep1 SED indicate the 5σ upper limits (calculated on the rms maps within a $0\farcs165$ radius circular aperture to best match the size within which the PSF fitting was done; see the Appendix). In F200W and the redder bands, the transient reached the maximum in Ep2 and then gradually faded.

4. Discussion

The NIRCam data used here were produced by only half of the NIRCam field of view (module B). Because of the different field orientations at different times, the area overlapped in all four epochs amounts to only 3.98 arcmin^2. Those data resulted in 14 robust transients, the largest number of transients ever found within such a small area. There are two reasons for this high transient production rate. First, the high sensitivity of NIRCam allows searching for transients to an unprecedented depth. The vast majority of our transients were fainter than 27.0 mag even at their peaks and were fainter than 28.0 mag most of the time in most bands. The PEARLS observations had exposure times of ∼0.8–1 hr per band per epoch, and the data reach 5σ limits of ∼28.5–30.0 mag (within a $0\farcs2$ radius aperture). This is deep enough to validate the transients in multiple bands. Second, M0416 includes two regions extremely magnified by the cluster, the Warhol and the Spock arcs, which are known to have produced a number of caustic transients in the previous studies with HST. Both arcs are at relatively low redshifts ($z \approx 1$), which facilitates the detection of luminous stars in them. In our data spanning 126 days, these two regions contributed seven and four transients, respectively,

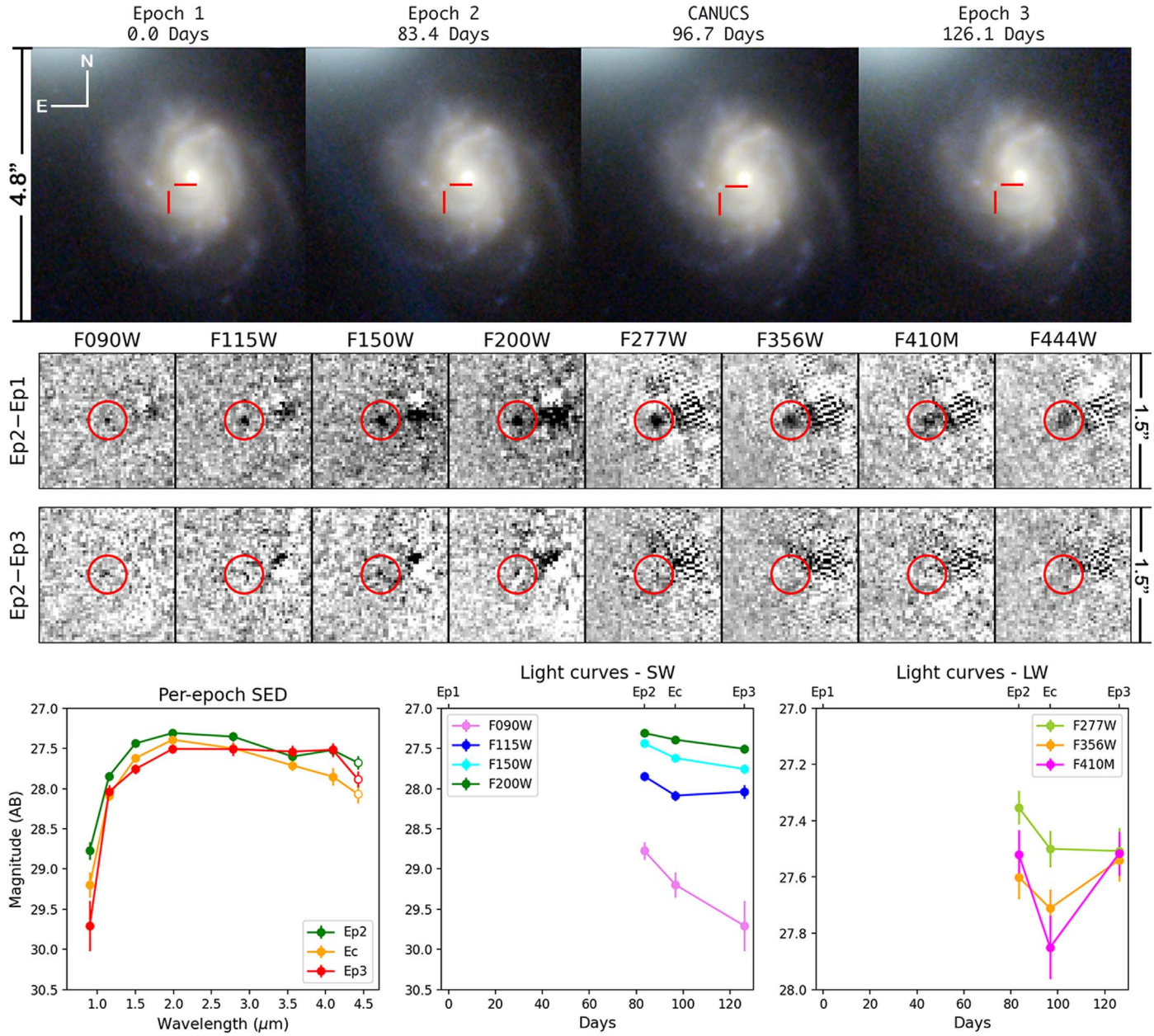

Figure 12. (Top row) Color images of SN02 in four epochs. Scale and orientation are labeled. The two red bars in each of the color images indicate SN02's location. It was not visible in Ep1. The host redshift is $z = 0.7093$. (Middle two rows) D21 and D23 (negative) difference images. The location of the source is indicated by the red circle ($0\farcs5$ radius) in each image. From the difference images involving Ep2, it seems that this transient reached the maximum in Ep2 and then faded. (Bottom row) SED evolution over four epochs (left panel) and the light curves in the SW bands (middle) and the LW bands (right).

making them the most productive transient *factories* known. In addition, our search found a transient in another arc (the Mothra arc) where no transient had been seen previously. As mentioned above (and to be discussed in detail in forthcoming papers), these transients are most likely stars in the lensed arcs that were temporarily magnified by an extra factor by microlensing. Studying such transients remains the only direct way to study individual stars at cosmological distances and therefore should be pursued by JWST in the coming years. These transients might occur very frequently. For example, `Dc2-W4` in the Warhol region appeared in Ec but was not seen in either Ep2 (13.6 days earlier) or Ep3 (29.4 days later). A monitoring cadence of ∼10 days (∼5 days in the rest frame) would potentially reveal more fast transients like `Dc2-W4`. This possibility is worth exploring with JWST in the near future.

In addition to the 12 transients in the highly magnified arcs, we also discovered two transients in regions that are only moderately magnified ($\mu \sim 2$–3). They are most likely SNe, and with intrinsic, post-peak brightnesses of ∼28.5 mag, they were bright enough to have been discovered even without the lensing magnification. Taken at face value, discovering two SNe in 3.98 arcmin^2 implies an SN surface density of ∼0.5 arcmin^{-2} integrated to $z \approx 2.2$ when monitored over ∼126 days. This frequency is broadly consistent with expectations (Wang et al. 2017; Regős & Vinkó 2019). Both SNe were caught near their maxima (in the rest frame visible range) by the Ep2 observations, which were taken 83.4 days after Ep1.

Owing to time dilation, neither transient changed significantly in brightness from Ep2 to Ec, which was 96.7 days after Ep1. This suggests that a time cadence of ∼90 days should be effective in discovering SN-like transients (integrated over all redshifts) and is likely to catch events near their peaks.

Finally, there could be a color bias in the transients reported here. The vast majority of them are very red with the only exception being SN01 in Ep1. Even that source transformed into a red object in Ep2. This may, at least in part, result from the initial selection being based on the F356W difference images. An initial selection based on an SW band (e.g., F150W) is possible, although it would be more complex to validate because of the more numerous defects in the SW data.

5. Summary

M0416 has been observed by NIRCam for four epochs, making it the field most intensely monitored by JWST in its Cycle 1. The eight-band data also provide the best near-IR SED sampling to date. This work has identified 14 transients in these four epochs, which spanned 126 days. Twelve transients occurred in three regions highly lensed by the cluster (seven, four, and one in the Warhol, Spock, and Mothra regions, respectively), while the other two happened in two background galaxies that are only moderately magnified (by ∼2–3×). The eight-band photometry enables the construction of the transients' SEDs from 0.9–4.4 μm. This is the first time that time-domain studies have such detailed information for interpretation. Further analysis of SEDs and light curves will be presented in forthcoming papers.

This work demonstrates the power of JWST in the study of the transient IR sky. It is now expected that JWST will be able to function for about 20 yr, enabling long-term monitoring programs addressing new science never before possible. A new era of IR time-domain science has begun.

The NIRCam data presented in this paper can be accessed via 10.17909/wmmd-ev74 after the respective proprietary periods.

Acknowledgments

This work is dedicated to the memory of our dear colleague Mario Nonino, a kind and gentle person and an example for many. We thank the CANUCS team for generously providing early access to their proprietary data of MACS0416. This project is based on observations made with the NASA/ESA/CSA JWST and obtained from the Mikulski Archive for Space Telescopes, which is a collaboration between the Space Telescope Science Institute (STScI/NASA), the Space Telescope European Coordinating Facility (ST-ECF/ESA), and the Canadian Astronomy Data Center (CADC/NRC/CSA). We thank our Program Coordinator, Tony Roman, for his expert help in scheduling this complex program. This research made use of Photutils, an Astropy package for the detection and photometry of astronomical sources. H.Y. and B.S. acknowledge the partial support from the University of Missouri Research Council Grant URC-23-029. J.M.D. acknowledges the support of project PGC2018-101814-B-100 (MCIU/AEI/MINECO/FEDER, UE) Ministerio de Ciencia, Investigación y Universidades. L.W. acknowledges support from NSF through grant #1813825. S.H.C., R.A.W., and R.A.J. acknowledge support from NASA JWST Interdisciplinary Scientist grants NAG5-12460, NNX14AN10G, and 80NSSC18K0200 from GSFC. ZM is supported in part by National Science Foundation grant #1636621. J.F.B. was supported by NSF grant No. PHY-2012955. C.N.A.W. acknowledges funding from the JWST/NIRCam contract NASS-0215 to the University of Arizona. C.C. is supported by the National Natural Science Foundation of China, Nos. 11803044, 12173045. A.Z. acknowledges support by grant No. 2020750 from the United States–Israel Binational Science Foundation (BSF), grant No. 2109066 from the United States National Science Foundation (NSF), and by the Ministry of Science & Technology, Israel.

Appendix

While we used isophotal aperture photometry by SExtractor to search for transients, we used PSF fitting for the final photometry of the transients identified. This approach assumes that transients are all point-like even at the JWST resolution, which should be valid. The reason we adopted the more complicated PSF fitting (as opposed to aperture photometry) was because of background contamination. Our transients were all embedded in highly nonuniform backgrounds, and in a lot of cases that still left structures even in the difference images between epochs. In such situations, PSF fitting handles contamination better than any aperture photometry. We did PSF fitting on the 30 mas images (as opposed to the 60 mas used in the transient identification). The process is outlined below.

We first generated the PSFs using the simulation tool `WebbPSF` (version 1.1.1) at the pixel scale of 30 mas. For each band, PSFs were simulated at 36 evenly distributed positions on each detector, and each simulated PSF was saved as an individual image. All simulated PSFs were 87×87 pixels ($2\farcs61 \times 2\farcs61$) in size. Then, effective PSFs, referred to as the WPSFs, were built using `EPSFBuilder` in `Photutils`. We also constructed empirical PSFs for comparison. The difficulty with those is that the M0416 field does not have many suitable stars. Nevertheless, we were able to find five isolated, unsaturated, and high-S/N stars for this purpose. A region of 87×87 pixels centered on each star was cut out from the image, and the five cutouts were sent to `EPSFBuilder` to build the empirical PSF, referred to as the EPSFs. Both types of PSFs were used, and we found only marginal differences (see below).

We used the `BasicPSFPhotometry` function in `Photutils` (Bradley et al. 2023) to perform PSF fitting. This function allows simultaneous fitting to multiple, overlapping sources when necessary. The nonlinear fitting routine `LevMarLSQFitter` in `Astropy` (Astropy Collaboration et al. 2013, 2018, 2022) was applied. The routine utilizes least-squares statistics to decide on the best fit. In PSF fitting, the actual area used to fit the model is usually much smaller than the full PSF size, as only the central region has sufficient S/N. Here we found that the optimal fitting area was 11×11 pixels, which is about 2.8× the FWHM of the F356W PSF.

We provided an initial guess of the source's centroid and flux when running the fit. The former was estimated by visually locating the peak pixel, while the latter was estimated by measuring the aperture flux within a circle of 11 pixels in diameter centered at the initial guess of the location. Tests showed that `BasicPSFPhotometry` could converge to the same solution even when the initial guesses were widely different. On the other hand, the routine requires an accurate background estimate because it fixes the background to the

input value. In most cases, we estimated the background by using the `MedianBackground` function in `Photutils` and adopting the 3σ clipped median in the image cutouts centered on the transient (i.e., the same image stamps as shown in the figures in the main text) with the sources masked.

Some special cases required tailored treatments of the fitting. For example, leaving both the source location and its flux as free parameters was not feasible for sources of low S/N. In these cases, we fixed the centroid and fit for the flux. For several sources in highly magnified regions, small but significant positional offsets were found between some SW and LW bands. In such cases, we did not force the fit to be centered at the same position; instead, we determined the centroid in different bands individually. As to the background estimate, median statistics were not applicable for sources in extremely nonuniform local backgrounds. For these cases, we estimated the local background value manually in an iterative manner: we subtracted different constants from the image at a step size of 0.005 MJy sr^{-1}, performed a PSF fit, and visually examined the residual image to determine the best local background value by eye. Sources that required some of these special treatments were:

1. D21-W2: We determined the source's centroids in the LW bands using the D21 images and in the SW bands using the D31 images. Their centroids in each band were then fixed for all epochs.
2. D21-W3: The source's centroids were determined from the D21 images and then fixed for Ec.
3. Dc2-W4: This source's local background is nonuniform, and we visually examined and selected the best local background value in Ec.
4. D31-W5/W6/W7: These sources' centroids in the SW bands were determined from the D31 F200W image. In the LW bands, they were determined from the D31 F356W image.
5. D21-S2: This source's centroids in the SW bands were determined from the F200W D21 image. In the LW bands, they were determined from the D21 F277W image.
6. D31-S4: This source's centroids in F115W and F150W were fixed to its F200W centroid.
7. Mothra (1) In Ep1, this source's centroid in F444W was fixed to its F410M centroid. (2) The complexity of simultaneously fitting two overlapping sources on a thin arc made it hard to use any automatic approach to estimate the local background. Therefore, we had to tune the background estimate manually as mentioned above. Furthermore, we used the Ep1 difference images between adjacent bands (the bluer image was always PSF matched to the redder image when constructing the difference) to judge whether the extracted flux in each band was reasonable under each step of the background estimate. For example, if the F150W–F115W difference image showed a distinct source at the transient location, it meant that the extracted flux in F150W must be higher than that in F115W. This added constraint, while tedious, allowed us to tweak the background values to obtain the most reasonable flux measurements.

In all cases, our PSF-fitting results have been properly normalized by aperture correction. As mentioned above, we used five stars to construct the EPSFs; these five stars were our basis for the aperture correction. We ran PSF fitting on these five stars to obtain their fitted fluxes and also derived their aperture fluxes within the same 11×11 pixel areas. The averaged ratio between the two in each band was the multiplicative aperture correction factor, which we applied to the outputs from `BasicPSFPhotometry`.

In the end, there are only marginal differences between the results based on the WPSFs and those based on the EPSFs. As the EPSFs were derived using only a small number of stars (a total of five), we regard them as being less secure. Therefore, we adopted the WSPF results for our final photometry reported in the tables.

ORCID iDs

Haojing Yan https://orcid.org/0000-0001-7592-7714
Zhiyuan Ma https://orcid.org/0000-0003-3270-6844
Bangzheng Sun https://orcid.org/0000-0001-7957-6202
Lifan Wang https://orcid.org/0000-0001-7092-9374
Patrick Kelly https://orcid.org/0000-0003-3142-997X
José M. Diego https://orcid.org/0000-0001-9065-3926
Seth H. Cohen https://orcid.org/0000-0003-3329-1337
Rogier A. Windhorst https://orcid.org/0000-0001-8156-6281
Rolf A. Jansen https://orcid.org/0000-0003-1268-5230
Norman A. Grogin https://orcid.org/0000-0001-9440-8872
John F. Beacom https://orcid.org/0000-0002-0005-2631
Christopher J. Conselice https://orcid.org/0000-0003-1949-7638
Simon P. Driver https://orcid.org/0000-0001-9491-7327
Brenda Frye https://orcid.org/0000-0003-1625-8009
Dan Coe https://orcid.org/0000-0001-7410-7669
Madeline A. Marshall https://orcid.org/0000-0001-6434-7845
Anton Koekemoer https://orcid.org/0000-0002-6610-2048
Christopher N. A. Willmer https://orcid.org/0000-0001-9262-9997
Aaron Robotham https://orcid.org/0000-0003-0429-3579
Jordan C. J. D'Silva https://orcid.org/0000-0002-9816-1931
Jake Summers https://orcid.org/0000-0002-7265-7920
Mario Nonino https://orcid.org/0000-0001-6342-9662
Nor Pirzkal https://orcid.org/0000-0003-3382-5941
Russell E. Ryan, Jr. https://orcid.org/0000-0003-0894-1588
Rafael Ortiz, III https://orcid.org/0000-0002-6150-833X
Scott Tompkins https://orcid.org/0000-0001-9052-9837
Rachana A. Bhatawdekar https://orcid.org/0000-0003-0883-2226
Cheng Cheng https://orcid.org/0000-0003-0202-0534
Adi Zitrin https://orcid.org/0000-0002-0350-4488
S. P. Willner https://orcid.org/0000-0002-9895-5758

References

Amanullah, R., Lidman, C., Rubin, D., et al. 2010, ApJ, 716, 712
Astropy Collaboration, Price-Whelan, A. M., Lim, P. L., et al. 2022, ApJ, 935, 167
Astropy Collaboration, Price-Whelan, A. M., Sipőcz, B. M., et al. 2018, AJ, 156, 123
Astropy Collaboration, Robitaille, T. P., Tollerud, E. J., et al. 2013, A&A, 558, A33
Balestra, I., Mercurio, A., Sartoris, B., et al. 2016, ApJS, 224, 33
Bergamini, P., Grillo, C., Rosati, P., et al. 2023, A&A, 674, A79
Bergamini, P., Rosati, P., Vanzella, E., et al. 2021, A&A, 645, A140
Bertin, E., & Arnouts, S. 1996, A&AS, 117, 393

Bradley, L., Sipőcz, B., Robitaille, T., et al., 2023 astropy/photutils: v1.8.0, Zenodo, doi:10.5281/zenodo.7946442
Bushouse, H., Eisenhamer, J., Dencheva, N., et al. 2023, JWST Calibration Pipeline, v1.9.4, Zenodo, doi:10.5281/zenodo.7577320
Caminha, G. B., Grillo, C., Rosati, P., et al. 2017, A&A, 600, A90
Chen, W., Kelly, P. L., Diego, J. M., et al. 2019, ApJ, 881, 8
Dawson, K. S., Aldering, G., Amanullah, R., et al. 2009, AJ, 138, 1271
Diego, J. M., Kei, Li, S., Meena, A. K., et al. 2023a, arXiv:2304.09222
Diego, J. M., Sun, B., Yan, H., et al. 2023b, A&A, 679, A31
Grillo, C., Rosati, P., Suyu, S. H., et al. 2018, ApJ, 860, 94
Grillo, C., Rosati, P., Suyu, S. H., et al. 2020, ApJ, 898, 87
Hayden, B., Rubin, D., Boone, K., et al. 2021, ApJ, 912, 87
Hoag, A., Huang, K. H., Treu, T., et al. 2016, ApJ, 831, 182
Kaurov, A. A., Dai, L., Venumadhav, T., Miralda-Escudé, J., & Frye, B. 2019, ApJ, 880, 58
Kelly, P. L., Chen, W., Alfred, A., et al. 2022, arXiv:2211.02670
Kelly, P. L., Diego, J. M., Rodney, S., et al. 2018, NatAs, 2, 334
Kelly, P. L., Rodney, S., Treu, T., et al. 2023a, ApJ, 948, 93
Kelly, P. L., Rodney, S., Treu, T., et al. 2023b, Sci, 380, abh1322
Kelly, P. L., Rodney, S. A., Treu, T., et al. 2015, Sci, 347, 1123
Kelly, P. L., Rodney, S. A., Treu, T., et al. 2016, ApJL, 819, L8
Lotz, J. M., Koekemoer, A., Coe, D., et al. 2017, ApJ, 837, 97
Regős, E., & Vinkó, J. 2019, ApJ, 874, 158
Riess, A. G., Rodney, S. A., Scolnic, D. M., et al. 2018, ApJ, 853, 126
Riess, A. G., Strolger, L.-G., Tonry, J., et al. 2004, ApJ, 607, 665
Rodney, S. A., Balestra, I., Bradac, M., et al. 2018, NatAs, 2, 324
Suzuki, N., Rubin, D., Lidman, C., et al. 2012, ApJ, 746, 85
Vanzella, E., Caminha, G. B., Rosati, P., et al. 2021, A&A, 646 A57
Vega-Ferrero, J., Diego, J. M., Miranda, V., & Bernstein, G. M. 2018, ApJL, 853, L31
Wang, L., Baade, D., Baron, E., et al. 2017, arXiv:1710.07005
Willott, C. J., Doyon, R., Albert, L., et al. 2022, PASP, 134, 025002
Windhorst, R. A., Cohen, S. H., Jansen, R. A., et al. 2023, AJ, 165, 13
Windhorst, R. A., Timmes, F. X., Wyithe, J. S. B., et al. 2018, ApJS, 234, 41
Yan, H., Ma, Z., Grogin, N., et al. 2023, TNSAN, 6, 1